Research Article Vol. 13, No. 11 / 1 Nov 2022 / *Biomedical Optics Express* 6153

Biomedical Optics EXPRESS

Integrating a pressure sensor with an OCT handheld probe to facilitate imaging of microvascular information in skin tissue beds

YAPING SHI,[1,3] JIE LU,[1,3] NHAN LE,[1] AND RUIKANG K. WANG[1,2,*]

[1] *Department of Bioengineering, University of Washington, Seattle, WA 98105, USA*
[2] *Department of Ophthalmology, University of Washington, Seattle, WA 98105, USA*
[3] *These authors contributed equally to this study*
[*] *wangrk@uw.edu*

Abstract: Optical coherence tomography (OCT) and OCT angiography (OCTA) have been increasingly applied in skin imaging applications in dermatology, where the imaging is often performed with the OCT probe in contact with the skin surface. However, this contact mode imaging can introduce uncontrollable mechanical stress applied to the skin, inevitably complicating the interpretation of OCT/OCTA imaging results. There remains a need for a strategy for assessing local pressure applied on the skin during imaging acquisition. This study reports a handheld scanning probe integrated with built-in pressure sensors, allowing the operator to control the mechanical stress applied to the skin in real-time. With real time feedback information, the operator can easily determine whether the pressure applied to the skin would affect the imaging quality so as to obtain repeatable and reliable OCTA images for a more accurate investigation of skin conditions. Using this probe, imaging of palm skin was used in this study to demonstrate how the OCTA imaging would have been affected by different mechanical pressures ranging from 0 to 69 kPa. The results showed that OCTA imaging is relatively stable when the pressure is less than 11 kPa, and within this range, the change of vascular area density calculated from the OCTA imaging is below 0.13%. In addition, the probe was used to augment the OCT monitoring of blood flow changes during a reactive hyperemia experiment, in which the operator could properly control the amount of pressure applied to the skin surface and achieve full release after compression stimulation.

1. Introduction

Optical coherence tomography (OCT) is a well-established imaging modality capable of providing high-resolution, three-dimensional (3D) and real-time imaging non-invasively [1]. Optical coherence tomography angiography (OCTA), as a powerful functional extension to the OCT, can provide functional blood vessel information without a need for contrast agents [2]. OCT and OCTA have now been translated to clinical ophthalmology [3–7], endoscopy [8–12] dentistry [13,14], neuroscience [15–17], and becomes more and more popular in dermatology [18–22]. Despite its attractiveness, there are several inherent issues in OCT/OCTA skin imaging acquisitions: a) unavoidable tissue motion; b) skin natural curve that leads to a difficulty to keep targeted region of interest within system available ranging distance; c) high scattering or specular reflection from the skin surface that can shadow the tissue information at deeper layers.

Previous studies have shown that a topical application of optical clearing agents (OCA), such as glycerin and ultrasound gel, can efficiently reduce scattering effect, thereby enhancing the light penetration depth and improving the imaging contrast [23–25]. Additionally, an OCT adapter cap with a glass window has been used to cover the scanning region during imaging acquisition to reduce the motion relative to the OCT probe, mitigate the skin natural curvature and suppress

#473013 https://doi.org/10.1364/BOE.473013
Journal © 2022 Received 11 Aug 2022; revised 22 Oct 2022; accepted 23 Oct 2022; published 1 Nov 2022

high backscattering from the skin surface [26–28]. While this approach demonstrated reasonable successes, the drawback is that the uncontrolled mechanical stress exerted on the skin inevitably impacts the skin optical property and blood perfusion, thereby affecting the OCT/OCTA imaging to an unknown degree [29]. Therefore, it is critically important to monitor and control the force or mechanical stress applied on the skin surface during OCT imaging when a glass window is used in the procedure. To achieve this, we aim to develop a built-in force sensor in an OCT handheld probe. For easy operation of the handheld probe, the built-in force sensor should be thin enough, sufficiently light, and provide real-time response.

Whilst there are many different force sensors available for use, we selected to use force-sensing resistors (FSR) in this study to be built into the OCT probe since they are compact, lightweight, cost-effective, and easily customizable [30]. FSRs have been widely incorporated into numerous biomechanical applications [31,32]. FSRs are composed of conductive polymers that exhibit a responsive relationship between resistance and mechanical force or pressure that is being applied [33]. Using a microcontroller, the change in its resistance can be interpreted within 1ms, allowing the applied pressure to be resolved in real-time.

In this study, we report a handheld scanning probe with built-in force sensors, allowing the operator to assess and monitor the external forces (therefore the pressure) applied on the skin during OCT imaging procedure. To demonstrate the potentials of pressure sensors in OCT imaging acquisition, we investigated how the pressure variations on the skin would have an effect on OCTA imaging as well as the blood flow real-time response to an application and subsequent release of the external force exerted on the skin, i.e., the well-known skin hyperemia experiment.

2. Method

2.1. Considerations and design of pressure sensor with the OCT probe

The demand to measure the pressure exerted on the skin surface during OCTA imaging acquisition arises from the need for imaging repeatability and reliability, aiming for quantitative assessment of microvascular responses under either disease or stimulation conditions. Uncontrolled pressure due to the contact of the glass window of the OCT probe with the skin surface can complicate the interpretation of subsurface microvascular information. To measure the force or pressure exerted on the skin surface, the most straightforward approach is to sandwich a force sensor between the skin and the round-glass window [34,35], i.e., the sensor in direct contact with skin . This requires the sensor material to be optically transparent and not interfere with the OCT probe beam. However, we did not find such a commercial off-the-shelf sensor that meets this requirement. To avoid the interference of the sensor with the optical beam, we decided to place three small FSRs equidistantly at the periphery of the round-glass window to form a ring shape, leaving the middle region of the glass window transparent for the light transmission. This design would not only solve the concern about OCT light passing, but also could reflect whether the force applied to the skin is uniform based on the distribution of pressures sensed by the three FSRs.

Another consideration is the use of OCAs (e.g., glycerin and ultrasound gel) for the purpose of refractive index matching with the skin [23]. If the sensors are in direct contact with skin, then the index matching gel would make the sensors prone to contamination. Therefore, we opted for a design where the force sensor is placed between the glass window and the probe, rather than having the sensor in direct contact with the skin. This design is reasonable because the force introduced by the contact of the glass window with the skin surface is approximately equal to the force between the glass window and the probe during imaging. A schematic of such design by taking the considerations above is shown in Fig. 1. To improve the flexibility, the design is made detachable and snap-on format so that it is applicable to a variety of OCT probes. Here, for the detachable attachment used in this study, it was customized to fit the LSM03 objective lens (Thorlabs Inc, USA) employed in the handheld probe of OCT system.

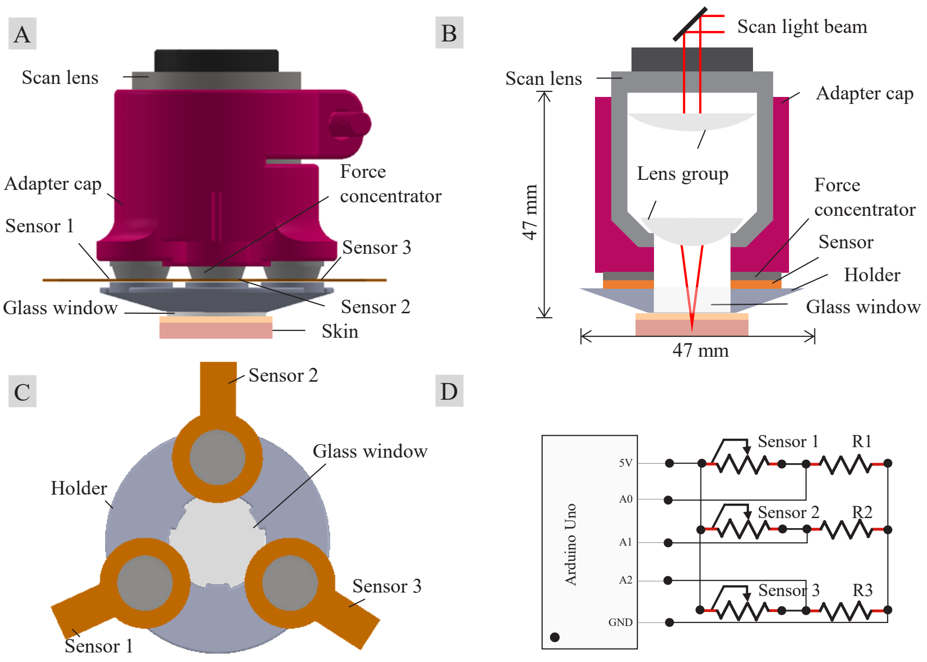

Fig. 1. *The design schematics of the detachable attachment integrated with force sensors.* (**A**) The overall design of the snap-on attachment that fits to the OCT probes. (**B**) The cross-sectional view of the design. (**C**) The perpendicular view at the level of the layout of three sensors, above the glass window, within the attachment. (**D**) Sensor resistance measurement and resistance-pressure conversion circuit, where R1 = R2 = R3 = 3.3kΩ.

The OCT system along with the handheld probe specially designed for skin imaging have been described in detail in our previous publications [26,36]. Here, we introduce the detachable attachment in some detail in this section. The customized attachment was used to adjust the distance between the objective lens and the skin surface. We integrated the force sensors into this attachment. As shown in Figs. 1(A) & 1(B), the snap-on attachment consists of : 1) a round-glass window (BK7 glass, 20mm diameter, 1mm in thickness, Micro-Store) that is situated at the distal end of the attachment, and its outer face would be in direct contact with the skin surface during imaging; 2) a base holder that is right above the glass window and acts a support for the attachment; 3) three force sensors (FSR 402 with a diameter of 12.7mm, Interlink Electronics Inc. [39]) that are located at the outer face of the base holder and placed equidistantly with a ring shape with a diameter of 42 mm at the periphery region, leaving a clear window in the center (diameter 20 mm) for imaging (Fig. 1(C)); 4) three force concentrators made of a kind elastic rubber ensure that the force loads are concentrated within the sensing area of the FSR and minimize the shear effects from non-normal loads, allowing the contact force to be evenly distributed across the force sensors to optimize sensor linearity and repeatability; and 5) a cap adapter that provides a tight-fit to the scan lens. The base holder and cap adapter were 3D printed to fit the size. Figures 1(B) and 1(C) show detailed layout of the attachment. Each FSR is connected in series with a reference resistor in the circuit (Fig. 1(D)) that converts the forces into electrical signals via an Arduino board (Arduino Uno, Arduino Store) that is fed into the proprietary OCT controlling software (in LabView platform) for real-time monitoring, documentation and display to aid the operator during imaging. The whole snap-on attachment is lightweight and compact (35 grams) and can be adapted for use in various OCT devices.

2.2. Sensor calibration

The resistance of the FSR force sensor decreases with the increase of contact force exerted on the active area. Figure 2(A) shows an overview of its typical response behavior for the force range between 0 to 10000 grams [39]. Considering the actual force applied to the skin that is relatively light, we chose the force range of interest between 100 and 1500 g (highlighted light-yellow in Fig. 2(A)) for calibration. Over this range, the relationship between the force (in grams) and resistance follows a power law characteristic [39,40] with:

$$F = k \cdot \frac{1}{R^x}\ , \tag{1}$$

where R is the measured resistance of force sensor when a force is applied on the active region, F represents the force (in grams), and k and x are calibration parameters that are dependent on the actual sensor characteristics. According to the circuit in Fig. 1(D), the resistance of the sensor, R, can be obtained following the equation:

$$R = R_i\left(\frac{V_{CC}}{V_{Ai}} - 1\right)\ . \tag{2}$$

where R_i $(i = 1,2,3)$ represents the reference resistance, V_{CC} is stimulation voltage, and V_{Ai} $(i = 1,2,3)$ is the measured voltage across the reference resistance.

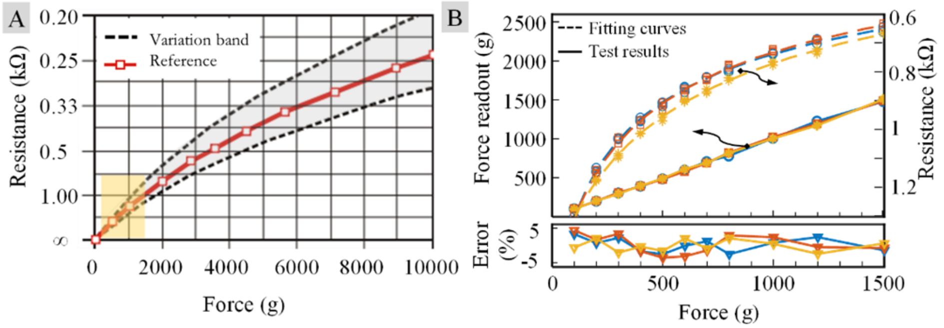

Fig. 2. *Sensor calibration.* **(A)** The force-resistance characteristics for the FSR sensor [39]. The shaded yellow square highlights the calibrated force range in this study. **(B)** Fitting curves from the calibration (dashed lines) to Eq. (1) to obtain the calibration parameters of k and x; and the measured forces from the sensor versus the applied known forces after the sensors are calibrated (solid lines). The triangles in the bottom graphs indicate the measurement errors after calibration.

The part-to-part variability of this type of pressure sensor is up to ±25%, highlighted by the dark dashed lines in Fig. 2(A). To mitigate the variability, each sensor was individually calibrated by fitting the relationship between the sensed resistance and the applied forces using Eq. (1) to find the parameter k and x. To perform the calibration, we added reference forces, F, to the sensor sequentially and recorded the resistance, R, of the sensor accordingly. For each sensor, three independent measurements were repeated at each reference force, and the average was taken to minimize the noise-induced variations. The parameters k and x were then obtained by fitting the reference forces and corresponding measured resistances under the force to the Eq. (1). After this calibration procedure, the sensors are ready to use in the OCT probe to provide real time readings and documentation of the pressure applied onto the skin surface.

2.3. OCT/OCTA imaging and participants

After the snap-on attachment was fabricated in the lab and calibrated, we tested its utility in the OCT/OCTA imaging using an in-house-built swept-source OCT (SS-OCT) system. The system employed a 200 kHz swept laser source (SL1310V1-10048, Thorlabs Inc.) with a central wavelength of 1310 nm and a bandwidth of 100 nm, giving an axial resolution of ~7 µm in air [26]. An LSM03 objective lens (Thorlabs Inc, USA) was used to deliver the light onto sample, giving a lateral resolution of ~25 µm according to Rayleigh criterion. With the probe beam delivered to the sample at ~5mW, the system had a measured signal to noise ratio at ~100dB. An OCTA imaging protocol was used to obtain OCTA images from the scanned tissue volume, where we acquired four repeated B-frames at each B-frame location to produce one blood flow B-scan using an algorithm termed as optical microangiography (OMAG) [37,38]. Each skin imaging volume covered a region of $\sim 8 \times 8 \times 1.5$ mm ($\sim 800 \times 800 \times 200$ pixels) in the x (fast axis), y (slow axis) and z (penetration into the skin) directions, respectively.

To investigate the likely impacts on OCTA imaging with different levels of mechanical stresses, we acquired 3D OCT/OCTA imaging of skin in human subjects. Before OCT/OCTA imaging, cleaning and disinfection on the imaging area were performed and then a drop of index matching liquid (glycerin) was applied to the skin surface to reduce the specular reflection effect on the final results [24]. Then, we sequentially increased the pressure applied to the skin, starting from no pressure to four strength levels (i.e., ~ 11, 17, 32, 69 kPa). When each strength level was stabilized, an OCT/OCTA image was captured. In order to test the repeatability of OCT/OCTA, we performed four sessions. Each session included five imaging points at different pressures (i.e., ~ 0, 11, 17, 32, 69 kPa) and a 15-minutes rest for a complete recovery of skin condition.

After obtaining OCT/OCTA data, we segmented each volume into three depth slabs measured from 245–392, 392–672, and 672–980 µm below the skin surface to compare the vascular response to external force stimulation at different depths. The tail-like artifacts from the strong forward scattering of erythrocytes would make vasculature at deep layers difficult to interpret, therefore, we utilized a previously published strategy to reduce such tailing artifacts [41–43]. For the visualization and quantification purposes, maximum intensity projection (MIP) *en face* imaging of the OCTA volume was generated from each slab. The OCTA was analyzed by using vessel area density (VAD) [44] extracted from the MIP *en face* imaging to indicate the repeatability of OCTA using an algorithm clinically validated in numerous ophthalmology studies, e.g. in [45]. The repeatability of OCTA imaging among different sessions was analyzed by using the intraclass correlation coefficient (ICC) [46].

Next, we investigated the utility of the proposed integrated probe on the well-known hyperemia experiment in skin. In a previous study on skin hyperemia [29], researchers induced force on the skin by manually adjusting the OCT probe but did not monitor or control the level of forces applied to the skin, resulting in inconsistent pressure being applied and incomplete pressure release, thereby increasing experiment bias and inevitable variations in the final results. This issue can be solved by using our proposed snap-on attachment that can provide the real-time information about the exact external force applied to the skin. While 3D OCTA scans can directly show the distribution of skin blood flow under different pressures, there remains an issue. That is, each 3D volume takes about 8 seconds, which would make it difficult to capture the peak hyperemia perfusion and recovery process after the release of mechanical stress. To mitigate this problem, we decided to use a repeated B-scan strategy, i.e. BM scan mode, instead of a 3D scan to demonstrate the reactive hyperemia features with the pressure stimulation. To achieve that, with the OCT system running at 285 frames per second, 30,000 repeated B-frames were continuously collected at the same location over a period of ~105 seconds. Over this period, the pressure was applied to start at the 8th second and gradually up to 70kPa over ~10 seconds, then stayed relatively stable for ~20 seconds, and finally released at the 38th second. Similar to 3D OCTA data processing, four consecutive OCT B-frames were collapsed into one OCTA

B-frames using the OMAG algorithm. In effect, each temporal dataset consisted of 7,500 OCTA B-frames with each B-frame consisting of 500 A-lines (covering ~8mm), allowing an OCTA imaging rate up to 71.25 frames per second. This imaging speed provides sufficient temporal resolution to observe blood volume response to the applied pressure changes.

Three volunteers were participated in this study for OCT imaging. The use of OCT laboratory equipment on human subjects was approved by the Institutional Review Board (IRB) of University of Washington. This study followed the tenets of the Declaration of Helsinki and was conducted in compliance with the Health Insurance Portability and Accountability Act. And written consent for imaging was obtained from each participant.

3. Results

3.1. Sensor performance

The force sensors were calibrated individually according to the description in Section 2.2 prior to assembling the attachment. Figure 2(B) shows the calibration results, where the dash lines show the fitting results for the FSRs resistance responses under the reference forces from 100 g to 1500 g using Eq. (1), with the three colors representing the three sensors used. The symbols on the dashed lines (circles, squares and asterisks) are the actual measured values (average from three trials) for the individual sensors. Such fitting gave the calibration parameters k and x for each sensor, which were then plugged in Eq. (1) to provide real time measurement of the force applied onto each sensor. After this calibration procedure, we tested the sensor readouts with a set of applied known forces. The results are given by the straight lines in Fig. 2(B), showing a linear relationship between the sensed results and the applied forces, where again the symbols of circles, squares and asterisks are the actual sensor readout values for each sensor. The regression for all the sensors indicated ($r = 0.99$ and $p \sim 0.0$), demonstrating an excellent linear relationship between the measured and the applied forces. The measurement error was also assessed less than 5% for each sensor, as shown in the bottom graph of Fig. 2(B).

After the calibration and assembly, the final pressure applied to the skin is obtained through dividing the sum of the forces detected from the three FSRs by the contact area of the glass window with the skin (i.e., 3.14 cm^2), and displayed on the computer screen in real time to guide the operators during imaging procedure. The process was faster (<1ms) than the acquisition time of a B frame image, which would meet the requirement of pressure analysis in most contact mode imaging applications. In addition, the pressures are also documented synchronously with the OCT/OCTA imaging for later analyses if necessary.

3.2. OCTA imaging changes with mechanical stress variations

Figure 3 shows a series of in vivo OCTA *en face* images (Figs.3 A-E) acquired from the palm skin site in a 31-year-old participant with a range of controlled pressures from 0kPa to 69kPa exerted on the skin surface, respectively. Because of 3D OCT/OCTA in nature, we also separated the microvascular information at the selected depths: 245-392µm (Figs.3 F-J), 392-672µm (Figs.3K-O) and 672-980µm (Figs.3 P-T), respectively, measured from the skin surface. In addition, to indicate the slab positions that were referenced for extracting the depth resolved vascular information, the selected OCTA B-frame images are given in Figs. 3 U-Y for information. Visually, capillary morphology without pressure (Figs. 3(A) and 3(U)) and with mild pressure at 11kPa (Figs. 3(B) and 3(V)) is similar and homogenous, suggesting that there is no apparent effect on the vasculature (at least for OCTA imaging) when the applied pressure is up to a level of 11 kPa in this subject. The change in VAD calculated from the MIP images was below 0.13%, indicating that stable and consistent OCTA images can be obtained with the pressure values less than 11 kPa. However, with the increase of pressure, the vascular density starts to diminish from a pressure level of 17 kPa (Figs. 3(C) and 3(W)), progressively to 32 kPa (Figs. 3(D) and 3(X)) and eventually the blood flow is almost ceased (within a tissue depth of ~1mm) at the level of 69 kPa (Figs. 3(E) and 3(Y)).

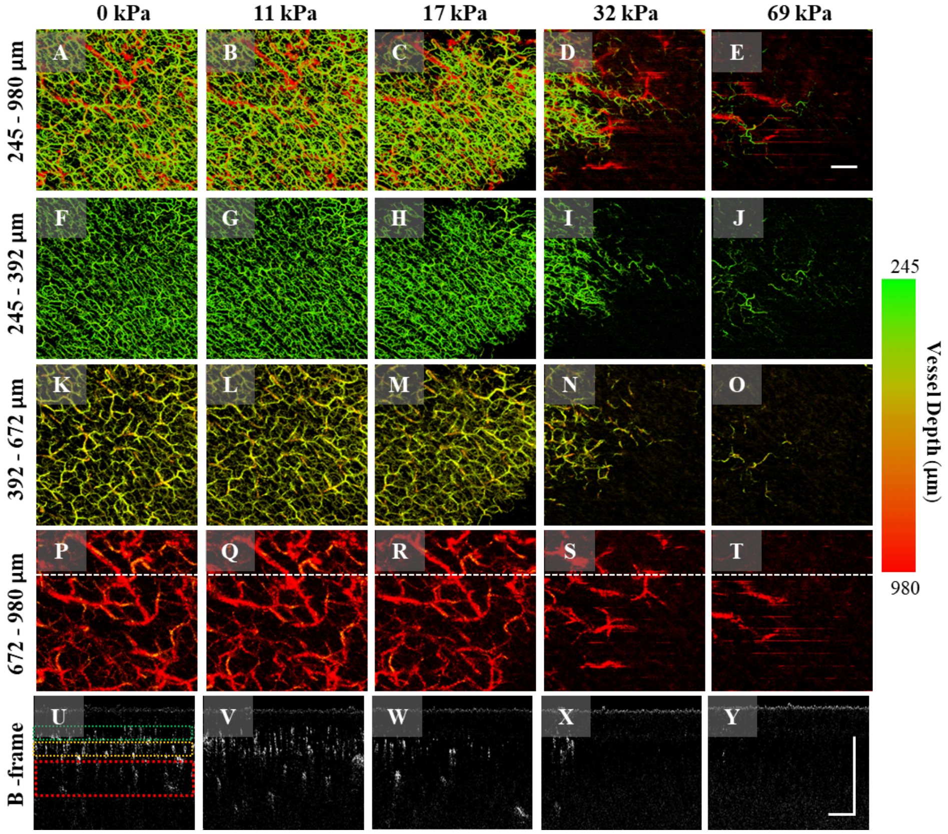

Fig. 3. The *changes in OCTA imaging upon the applied pressures on the skin surface*. (**A-E**) the *en face* OCTA maps of the whole skin depth from 245-980 µm under the pressure of 0, 11, 17, 32, 69, respectively, as shown. **(F-J)** the same as in (A-E) but the selected slab depth of 245–392 µm. **(K-O)** the same as in (A-E) but the selected slab depth of 392–672 µm. (**P-T**) the same as in (A-E) but the selected slab depth of 672-980µm. (**U-Y**) representative OCTA B-scans at the position marked as dashed white line in (P-T), where the green square indicates the depth of 245–392 µm below the surface; the yellow square indicates the depth of 392-672 µm below the surface; and the red square indicates the depth of 672-980 µm below the surface. All *en face* vascular maps were produced by maximum intensity projection. Color bar represents vessel depth. Scale bar represents 1 mm

From the depth resolved OCTA images, the response trend of the blood vessels in each layer to the applied pressure is similar to that of the whole layer (i.e., 245–980 µm from the surface). The top layer of the dermis (Figs. 3(F)-(J)) appeared to undergo more obvious changes after external force stimulation than the other two layers (Figs. 3(K)-(O), and Figs. 3(P)-(T)). This may be due to small capillaries being more sensitive to external pressure changes. Figure 4 shows the quantitative comparisons of VAD under different pressures, corresponding to the appearance of OCTA images shown in Fig. 3. In addition, the repeatability study showed that all ICCs of the VAD derived from the OCTA imaging were greater than 0.90 (Table 1), indicating an excellent repeatability of OCTA imaging [46].

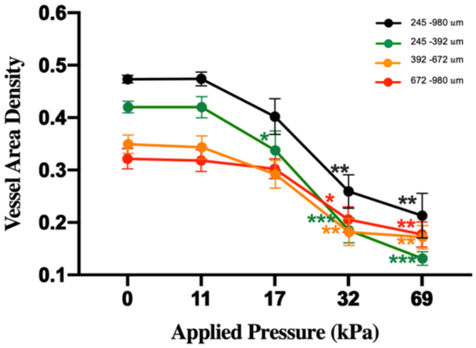

Fig. 4. The alteration in vessel area density (VAD) upon the applied pressures. The curves shown are from the whole skin depth (245 - 980 µm), and the slab depths of 245-392 µm, 392-672 µm and 672-980 µm, respectively. Error bar represents standard deviation from four sessions. *, P value < 0.05; **, P value < 0.01; ***, P value < 0.001.

Table 1. Intraclass correlation coefficient (ICC) among the four tested sessions.

Depth (µm)	245-980	245-392	392-672	672-980
Intraclass Correlation Coefficient (ICC)	0.946	0.971	0.933	0.908

As expected, our study demonstrated a strong correlation between the applied stress and OCTA imaging appearance (Fig. 3) and quantification (Fig. 4). In general, the compression of skin results in the reduction of skin blood flow, interstitial fluids, skin thickness and closer packing of tissue components [23,47], which leads to an alteration in the tissue optical property [48]. Here, for OCTA imaging, blood flow reduction is more dominant than other effects on imaging quality. Even though we applied a uniformly distributed pressure to the skin surface, the appearance of the blood vessels exhibited heterogeneous at pressures of 32 kPa and 69 kPa. It might be because of uneven topology of the tissue surface and heterogeneous content of tissue. Previous studies extracted the optical property of the skin, such as optical attenuation coefficient (OAC) [49–52], tissue mechanical [53–56] and birefringent information [20,21], to assess wound healing [57] and skin tension lines [58] by using OCT, however the results were interpretative without the consideration of the potential impact of the compression on the skin. We expect that with the help of pressure sensors during imaging, these measurements would be more reliable and repeatable, giving rise to more accurate interpretation of the final results.

3.3. Application of pressure sensors in the hyperemia experiment

Figure 5 shows the changes in the blood flow in the palm skin tissue beds after the application of external force (up to ~ 70kPa) and subsequent release. Figure 5(A) is an *en face* OCTA image that was used to guide the repeated scanning protocol, where the dashed line indicates the location to acquire temporal OCT (Fig. 5(B)) and OCTA B-scans (Fig. 5(C)). From the temporal OCTA B-scans, the blood flow was assessed from a slab region of interest that was segmented from 245 to 980 µm measured from the surface as marked by dashed box in Fig. 5(C). Figure 5(D) is resulted from the MIP projection of this selected slab to indicate the temporal blood flow response at the B-scan cross-section to the applied pressure and then release. To facilitate the visualization, we summed the OCTA blood flow signals within the slab region of interest at each B-scan (to indicate the blood volume), and then plot after the normalization against the time (Fig. 5(E)), where the pressure measured by the sensors is also plotted alongside for comparison. Both the results (Figs. 5(D) and 5(E)) demonstrate that the blood volume first decreased due to the external pressure, then produced reactive hyperemic perfusion right after the subsequent release of external force at the 38th second, and finally returned to the baseline level. In addition, we observed that besides the variations, the blood flow seemed to fluctuate periodically, likely due to the pulsatile nature of the blood. To confirm, we performed a Fourier transformation on Fig. 5(E). Figure 5(D) is the calculated frequency spectrum, showing a characteristic frequency peak at ~1.1 Hz (highlighted by the red asterisk) that was matched well with the heart rate of the subject (measured separately by a heart rate monitor), confirming that such fluctuations in blood volume is caused by pulsatile blood movement within the vascular tree. Figure 5(G) is the magnified view of a selected time window of ~ 3s in Fig. 5(E), where the periodic pattern with minor local fluctuations is evident that resembles the pulsatile waveform, typically seen in clinic. Meanwhile, the shape of the periodic pattern is also observed to slightly vary under different pressures (Fig. 5(E)).

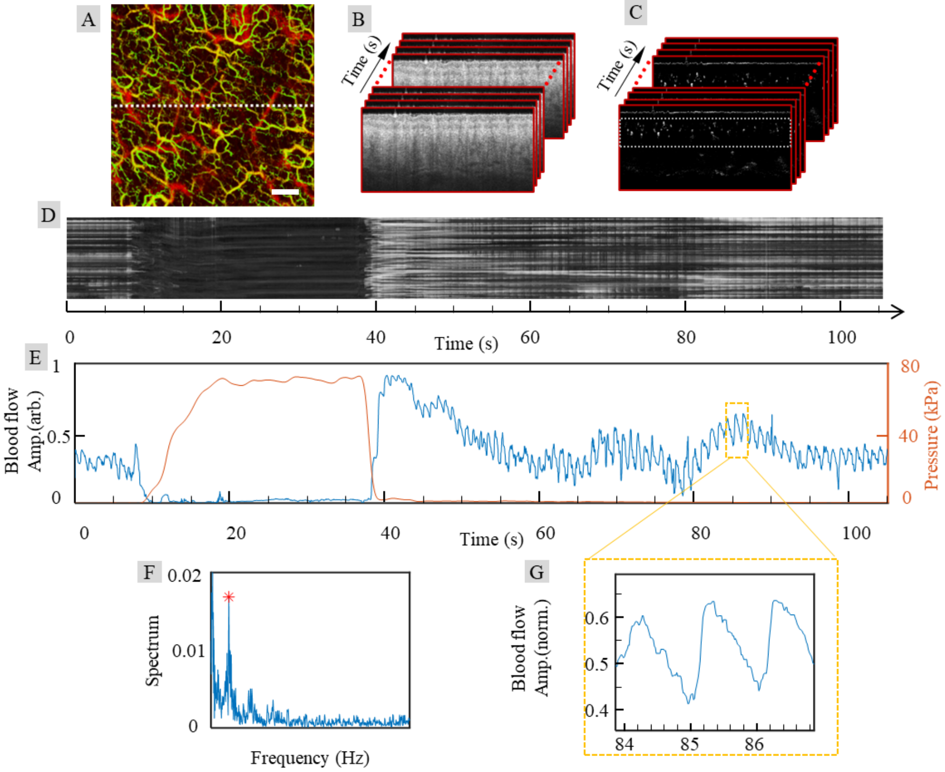

Fig. 5. The blood flow response to the application and subsequent release of external force to simulate the reactive hyperemia experiments. (**A**) The *en face* OCTA map under no pressure that was used to guide the repeated B-scans to generate temporal blood flow signals, where the dashed line indicates the location of the time series of repeated B-scans. The scale bar represents 1 mm. (**B**) the illustration of collected time series of OCT B-scans and **(C)** corresponding temporal OCTA B-scans where the selected slab region of interested is marked by white dashed box. (**D**) Maximum intensity OCTA projection from the region of interest shown in (C) over 105-second repeated B-scans. **(E)** the blue trace indicates the time series of blood flow signals that was obtained by summing the OCTA signals within the region of interest at each B-scan shown in (C). The measured pressures (light red color) during the entire experiment are plotted alongside with the blood flow signal for easy comparison. (**F**) The frequency power of the time series of blood flow signals in (E). The red asterisk indicates the pulsatile component that is measured at 1.1 Hz. (**G**) Magnified image of the selected time window of ~3s highlighted in the dashed rectangles shown in (E).

The reason for the reactive hyperemia is that the localized pressure applied to the skin activates a large number of cutaneous receptors, leading to vasodilation that gives rise to an increase of skin blood flow. This response can protect skin from ischemia during pressure stimulation [59].

However, some conditions, such as diabetes [60], hypertension [61], aging [62] and atherosclerosis [63], can impair this protective mechanism of the microvasculature. Therefore, reactive hyperemia may be utilized as a biological indicator with respect to peripheral microvascular function [64]. Wang-Evers et al. [3] reported that OCT imaging had the ability to provide functional information of the microvasculature related to age and blood pressure that might help assess overall vascular health. However, uncontrolled pressure applied to the skin during the experiment may add the burden to the already traumatized skin microvasculature and lead to inaccurate experimental results. Moreover, Xie et al. [65] and Gong et al [27]. reported that OCTA can be used to detect microvascular pulsatility in the peripheral circulation in human skin, in which waveforms are similar to Fig. 5(E). These two prior studies did not mention the influence of external pressures on the pulsatile waveforms. However, we did observe that such waveform shapes varied under different external pressures. It could be argued that when performing the hyperemia and pulsatile experiment, pressure sensors may be required to help control the external pressure during OCT imaging acquisition. While the observations of blood responses to the applied pressure are sufficiently interesting and may be explored to further our understanding of reactive hyperemia in normal and diseased conditions, the investigation of their physiological meaning or clinical relevance is beyond the scope of the current study. Here, we focused on introducing an augmented pressure sensor during imaging so that the applied level of pressure onto the skin surface can be precisely controlled and monitored.

4. Discussion and conclusions

In the OCT/OCTA imaging of skin, the use of a glass window in contact with skin has become a good practice. This strategy aims for obtaining repeatable and quality images to facilitate the quantification effort through mitigating tissue motion relative to the OCT probe and minimizing the specular reflections from the skin surface. While efficient, this method can inevitably introduce uncontrollable mechanical stress on the skin surface, leading to an alteration of the skin optical property which could affect the measurement/imaging of functional microvascular flows within skin tissue beds. Such effect would in turn give rise to the complications in the interpretation of the OCT/OCTA results. Despite of this issue, several research groups have utilized OCT together with this strategy to analyze reactive hyperemia [29], pulsatile waveforms [27,65], and blood glucose [47], where the skin contact introduced mechanical pressure was unfortunately not controlled, nor documented. Therefore, there is clearly a need for the monitoring and control of the applied pressure on the skin surface during OCT/OCTA imaging acquisition. To the best of the authors' knowledge, the work presented in this study demonstrates for the very first time the ability of pressure sensors to aid in acquiring reliable OCT/OCTA images. A handheld OCT probe combined with built-in force sensors was developed and its potential for skin imaging was demonstrated. With the pressure values provided by the force sensors in real time, an operator can easily determine whether the pressure applied to the skin is within an acceptable range that would not affect OCTA imaging of microvascular information and help to obtain repeatable OCTA images for later quantification purpose. Moreover, when performing reactive hyperemia experiments, the real time monitoring of the applied pressure on the skin would provide a key maneuver information that can guide the operator to properly conduct a successful experiment.

Although the current development of an augmented snap-on attachment to the OCT probe is useful in providing the operators with controlled pressure on the skin surface, it should be noted that there are several limitations in our study. Firstly, the FSR integrated in the OCT probe has lower accuracy than other types of force sensors, such as load cells or strain gauges [66]. However, these other types of sensors are not as compact as FSRs. It is also worth noting that the precise assessment of the pressure applied on the skin is not the goal of the built-in force sensors. Our current development is merely aimed to provide the operator with a controlled level of skin pressure so as to obtain consistent and reliable OCT/OCTA imaging that can provide meaningful quantification results of microvascular information within skin tissue beds. We believe that the precisions of the chosen FSR sensors are sufficient to monitor noticeable changes in microvascular information upon the application of the external forces on the skin surface. Secondly, we only investigated the effect of pressure on OCTA imaging. To further demonstrate the potentials of pressure sensors in future studies, some other optical properties based on OCT imaging, such as optical attenuation, biomechanical and birefringent properties of the interrogated tissue, could also be analyzed and compared at different pressures under the guidance of the pressure sensor, so that more accurate results can be obtained by removing the possible complications of the contact effect from the interpretation of results. Thirdly, the experiments in this study were only performed on the palm skin, therefore, results are not representative of the skin reaction at other body sites. Based on our previous experiences, facial skin is more sensitive to external pressure compared to the palm skin, while the abdomen skin does seem to be less sensitive to external pressures. However, the goal of study is aimed at showing the usefulness of real time monitoring of the pressure exerted on the skin surface in order to obtain reproducible and reliable OCT/OCTA skin images.

In summary, we have successfully developed built-in pressure sensors in an OCT handheld probe and demonstrated the application of the pressure sensor in the skin OCTA research. Continued investigations using the technology discussed herein will aid researchers/clinicians in the betterment of OCT/OCTA data acquisition in future.

Funding. Research to Prevent Blindness; Washington Research Foundation.

Acknowledgments. Research supported in part by an unrestricted grant from the Research to Prevent Blindness, Inc., New York, NY, and Washington Research Foundation. The funding organization had no role in the design or conduct of this research.

Disclosures. Dr. Wang discloses intellectual property owned by the Oregon Health and Science University and the University of Washington. Dr. Wang also receives research supports from Carl Zeiss Meditec, Inc., Colgate Palmolive Company and Facebook technologies LLC. He is a consultant to Carl Zeiss Meditec Inc. All other authors have no disclosures.

Data availability. Data underlying the results presented in this paper are not publicly available at this time but may be obtained from the authors upon reasonable request.

References

1. P. H. Tomlins and R. K. Wang, "Theory, developments and applications of optical coherence tomography," J. Phys. D: Appl. Phys. **38**(15), 2519–2535 (2005).
2. C.-L. Chen and R. K. Wang, "Optical coherence tomography based angiography [Invited]," Biomed. Opt. Express **8**(2), 1056–1082 (2017).
3. A. H. Kashani, C.-L. Chen, J. K. Gahm, F. Zheng, G. M. Richter, P. J. Rosenfeld, Y. Shi, and R. K. Wang, "Optical coherence tomography angiography: a comprehensive review of current methods and clinical applications," Prog. Retinal Eye Res. **60**, 66–100 (2017).
4. J. Wang, T. T. Hormel, L. Gao, P. Zang, Y. Guo, X. Wang, S. T. Bailey, and Y. Jia, "Automated diagnosis and segmentation of choroidal neovascularization in OCT angiography using deep learning," Biomed. Opt. Express **11**(2), 927–944 (2020).
5. E. Tang, M. T. El-Haddad, S. N. Patel, and Y. K. Tao, "Automated instrument-tracking for 4D video-rate imaging of ophthalmic surgical maneuvers," Biomed. Opt. Express **13**(3), 1471–1484 (2022).
6. T. Adejumo, T. H. Kim, D. Le, T. Son, G. Ma, and X. Yao, "Depth-resolved vascular profile features for artery-vein classification in OCT and OCT angiography of human retina," Biomed. Opt. Express **13**(2), 1121–1130 (2022).
7. H. Zhou, J. Liu, R. Laiginhas, Q. Zhang, Y. Cheng, Y. Zhang, Y. Shi, M. Shen, G. Gregori, P. J. Rosenfeld, and R. K. Wang, "Depth-resolved visualization and automated quantification of hyperreflective foci on OCT scans using optical attenuation coefficients," Biomed. Opt. Express **13**(8), 4175–4189 (2022).
8. L. Qi, Z. Zhuang, S. Zhang, S. Huang, Q. Feng, and W. Chen, "Automatic correction of the initial rotation angle error improves 3D reconstruction in endoscopic airway optical coherence tomography," Biomed. Opt. Express **12**(12), 7616–7631 (2021).
9. G. Yang, E. Mehanna, C. Li, H. Zhu, C. He, F. Lu, K. Zhao, Y. Gong, and Z. Wang, "Stent detection with very thick tissue coverage in intravascular OCT," Biomed. Opt. Express **12**(12), 7500–7516 (2021).

10. Z. Yang, S. Soltanian-Zadeh, K. K. Chu, H. Zhang, L. Moussa, A. E. Watts, N. J. Shaheen, A. Wax, and S. Farsiu, "Connectivity-based deep learning approach for segmentation of the epithelium in in vivo human esophageal OCT images," Biomed. Opt. Express **12**(10), 6326–6340 (2021).
11. H. Sun, C. Zhao, Y. Qin, C. Li, H. Jia, B. Yu, and Z. Wang, "In vivo detection of plaque erosion by intravascular optical coherence tomography using artificial intelligence," Biomed. Opt. Express **13**(7), 3922–3938 (2022).
12. D. Adams, A. Majid, and M. J. Suter, "Polarization mode dispersion correction in endoscopic polarization-sensitive optical coherence tomography with incoherent polarization input states," Biomed. Opt. Express **13**(6), 3446–3460 (2022).
13. P. Tang, N. Le, J. Lu, K. H. Chung, H. Subhash, L. Kilpatrick-Liverman, and R. K. Wang, "Local axis orientation mapped by polarization sensitive optical coherence tomography provides a unique contrast to identify caries lesions in enamel," Biomed. Opt. Express **13**(8), 4247–4260 (2022).
14. N. Le, J. Lu, P Tang, K.H. Chung, H. Subhash, L. Kilpatrick-Liverman, and R.K. Wang, "Intraoral optical coherence tomography and angiography combined with autofluorescence for dental assessment," Biomed. Opt. Express **13**(6), 3629–3646 (2022).
15. M. Ibne Mokbul, "Optical coherence tomography: basic concepts and applications in neuroscience research," J. Med. Eng. **2017**, 1–20 (2017).
16. A. A. Moiseev, K. A. Achkasova, E. B. Kiseleva, K. S. Yashin, A. L. Potapov, E. L. Bederina, S. S. Kuznetsov, E. P. Sherstnev, D. V. Shabanov, G. V. Gelikonov, Y. V. Ostrovskaya, and N. D. Gladkova, "Brain white matter morphological structure correlation with its optical properties estimated from optical coherence tomography (OCT) data," Biomed. Opt. Express **13**(4), 2393–2413 (2022).
17. J. Liu, W. Ammon, R.J. Jones, J. Nolan, R.P. Wang, S. Chang, M.P. Frosch, A. Yendiki, D. Boas, C. Magnain, B. Fischl, and H. Wang, "Refractive-index matching enhanced polarization sensitive optical coherence tomography quantification in human brain tissue," Biomed. Opt. Express **13**(1), 358–372 (2022).
18. J. Welzel, "Optical coherence tomography in dermatology: a review," Skin Res. Technol. **7**(1), 1–9 (2001).
19. J. Ogien, O. Levecq, H. Azimani, and A. Dubois, "Dual-mode line-field confocal optical coherence tomography for ultrahigh-resolution vertical and horizontal section imaging of human skin in vivo," Biomed. Opt. Express **11**(3), 1327–1335 (2020).
20. X. Zhou, S. Maloufi, D. C. Louie, N. Zhang, Q. Liu, T. K. Lee, and S. Tang, "Investigating the depolarization property of skin tissue by degree of polarization uniformity contrast using polarization-sensitive optical coherence tomography," Biomed. Opt. Express **12**(8), 5073–5088 (2021).
21. W. C. Lin, R. A. Byers, W. Li, S. G. Danby, M. J. Cork, and S. J. Matcher, "Imaging striae distensae: a comparison between PS-OCT and digital dermoscopy," Biomed. Opt. Express **12**(6), 3296–3311 (2021).
22. J. Lu, A. J. Deegan, Y. Cheng, S. P. Mandell, and R. K. Wang, "OCT-based angiography and surface topography in burn-damaged skin," Lasers Surg. Med. **53**(6), 849–860 (2021).
23. D. Zhu, K. V. Larin, Q. Luo, and V. V. Tuchin, "Recent progress in tissue optical clearing," Laser Photonics Rev. **7**(5), 732–757 (2013).
24. X. Xu and R. K. Wang, "Synergistic effect of hyperosmotic agents of dimethyl sulfoxide and glycerol on optical clearing of gastric tissue studied with near infrared spectroscopy," Phys. Med. Biol. **49**(3), 457–468 (2004).
25. X. Xu and R. K. Wang, "The role of water desorption on optical clearing of biotissue: studied with near infrared reflectance spectroscopy," Med. Phys. **30**(6), 1246–1253 (2003).
26. J. Xu, S. Song, S. Men, and R. K. Wang, "Long ranging swept-source optical coherence tomography-based angiography outperforms its spectral-domain counterpart in imaging human skin microcirculations," J. Biomed. Opt. **22**(11), 1 (2017).
27. P. Gong, C. Heiss, D. M. Sampson, Q. Wang, Z. Yuan, and D. D. Sampson, "Detection of localized pulsatile motion in cutaneous microcirculation by speckle decorrelation optical coherence tomography angiography," J. Biomed. Opt. **25**(09), 095004 (2020).
28. P. Gong, S. Es'haghian, K.-A. Harms, A. Murray, S. Rea, B. F. Kennedy, F. M. Wood, D. D. Sampson, and R. A. McLaughlin, "Optical coherence tomography for longitudinal monitoring of vasculature in scars treated with laser fractionation," J. Biophotonics **9**(6), 626–636 (2016).
29. M. Wang-Evers, M. J. Casper, J. Glahn, T. Luo, A. E. Doyle, D. Karasik, A. C. Kim, W. Phothong, N. R. Nathan, T. Heesakker, G. Kositratna, and D. Manstein, "Assessing the impact of aging and blood pressure on dermal microvasculature by reactive hyperemia optical coherence tomography angiography," Sci. Rep. **11**(1), 13411 (2021).
30. S. Parmar, I. Khodasevych, and O. Troynikov, "Evaluation of flexible force sensors for pressure monitoring in treatment of chronic venous disorders," Sensors **17**(8), 1923 (2017).
31. G. S. Faber, A. S. Koopman, I. Kingma, C. C. Chang, J. T. Dennerlein, and J. H. van Dieën, "Continuous ambulatory hand force monitoring during manual materials handling using instrumented force shoes and an inertial motion capture suit," J. Biomech. **70**, 235–241 (2018).
32. J. S. Schofield, K. R. Evans, J. S. Hebert, P. D. Marasco, and J. P. Carey, "The effect of biomechanical variables on force sensitive resistor error: Implications for calibration and improved accuracy," J. Biomech. **49**(5), 786–792 (2016).
33. S. Stassi, V. Cauda, G. Canavese, and C. F. Pirri, "Flexible tactile sensing based on piezoresistive composites: A review," Sensors **14**(3), 5296–5332 (2014).

34. K. M. Kennedy, S. Es'haghian, L. Chin, R. A. McLaughlin, D. D. Sampson, and B. F. Kennedy, "Optical palpation: optical coherence tomography-based tactile imaging using a compliant sensor," Opt. Lett. **39**(10), 3014–3017 (2014).
35. P. Wijesinghe, D. D. Sampson, and B. F. Kennedy, "Computational optical palpation: a finite-element approach to micro-scale tactile imaging using a compliant sensor," J. R. Soc. Interface. **14**(128), 20160878 (2017).
36. A. Deegan, J. Lu, R. Sharma, S. Mandell, and R. Wang, "Imaging human skin autograft integration with optical coherence tomography," Quant. Imaging Med. Surg. **11**(2), 784–796 (2021).
37. R. K. Wang, L. An, P. Francis, and D. J. Wilson, "Depth-resolved imaging of capillary networks in retina and choroid using ultrahigh sensitive optical microangiography," Opt. Lett. **35**(9), 1467–1469 (2010).
38. L. An, J. Qin, and R. K. Wang, "Ultrahigh sensitive optical microangiography for in vivo imaging of microcirculations within human skin tissue beds," Opt. Express **18**(8), 8220–8228 (2010).
39. , "FSR Integration Guide - [PDF Document]," https://documents.pub/document/fsr-integration-guide.html.
40. J. McNeill, M. Crivello, Y. Mendelson, D. Sen, R. Dunn, and K. Hickle, "Flexible sensor for measurement of skin pressure and temperature in a clinical setting," in *2016 IEEE SENSORS* (2016), pp. 1–3. doi: 10.1109/ICSENS.2016.7808600.
41. A. Zhang, Q. Zhang, and R. K. Wang, "Minimizing projection artifacts for accurate presentation of choroidal neovascularization in OCT micro-angiography," Biomed. Opt. Express **6**(10), 4130–4143 (2015).
42. U. Baran, W. J. Choi, Y. Li, and R. K. Wang, "Tail artifact removal in OCT angiography images of rodent cortex," J. Biophotonics **10**(11), 1421–1429 (2017).
43. Q. Zhang, A. Zhang, C. S. Lee, A. Y. Lee, K. A. Rezaei, L. Roisman, A. Miller, F. Zheng, G. Gregori, M. K. Durbin, L. An, P. F. Stetson, P. J. Rosenfeld, and R. K. Wang, "Projection artifact removal improves visualization and quantitation of macular neovascularization imaged by optical coherence tomography angiography," Ophthalmology retina **1**(2), 124–136 (2017).
44. Z. Chu, J. Lin, C. Gao, C. Xin, Q. Zhang, C.-L. Chen, L. Roisman, G. Gregori, P. J. Rosenfeld, and R. K. Wang, "Quantitative assessment of the retinal microvasculature using optical coherence tomography angiography," J. Biomed. Opt **21**(6), 066008 (2016).
45. A. Y. Kim, Z. Chu, A. Shahidzadeh, R. K. Wang, C. A. Puliafito, and A. H. Kashani, "Quantifying microvascular density and morphology in diabetic retinopathy using spectral-domain optical coherence tomography angiography," Invest. Ophthalmol. Visual Sci. **57**(9), OCT362 (2016).
46. M. E. Wolak, D. J. Fairbairn, and Y. R. Paulsen, "Guidelines for estimating repeatability," Methods Ecol. Evol. **3**(1), 129–137 (2012).
47. V. V. Sapozhnikova, R. V. Kuranov, I. Cicenaite, R. O. Esenaliev, and D. S. P. Prough, "Effect on blood glucose monitoring of skin pressure exerted by an optical coherence tomography probe," J. Biomed. Opt. **13**(2), 021112 (2008).
48. E. K. Chan, B. Sorg, D. Protsenko, M. O'Neil, M. Motamedi, and A. J. Welch, "Effects of compression on soft tissue optical properties," IEEE J. Select. Topics Quantum Electron. **2**(4), 943–950 (1996).
49. S. Chang and A. K. Bowden, "Review of methods and applications of attenuation coefficient measurements with optical coherence tomography," J Biomed Opt **24**(2019).
50. B. Ghafaryasl, K. Vermeer, J. Kalkman, T. Callewaert, J. de Boer, and L. van Vliet, "Attenuation coefficient estimation in Fourier-domain OCT of multi-layered phantoms," Biomed. Opt. Express **12**(5), 2744–2758 (2021).
51. K. Li, W. Liang, Z. Yang, Y. Liang, and S. Wan, "Robust, accurate depth-resolved attenuation characterization in optical coherence tomography," Biomed. Opt. Express **11**(2), 672–687 (2020).
52. M. Hohmann, B. Lengenfelder, D. Muhr, M. Späth, M. Hauptkorn, F. Klämpfl, and M. Schmidt, "Direct measurement of the scattering coefficient," Biomed. Opt. Express **12**(1), 320–335 (2021).
53. D. Bronte-Ciriza, J. S. Birkenfeld, A. de la Hoz, A. Curatolo, J. A. Germann, L. Villegas, A. Varea, E. Martínez-Enríquez, and S. Marcos, "Estimation of scleral mechanical properties from air-puff optical coherence tomography," Biomed. Opt. Express **12**(10), 6341–6359 (2021).
54. Y. Zhang, Y. Ling, D. Zhang, M. Wang, C. Purslow, Y. Yang, C. Li, and Z. Huang, "Quantitative measurement of mechanical properties in wound healing processes in a corneal stroma model by using vibrational optical coherence elastography (OCE)," Biomed. Opt. Express **12**(1), 588–603 (2021).
55. J. Li, M. S. Hepburn, L. Chin, A. Mowla, and B. F. Kennedy, "Analysis of sensitivity in quantitative micro-elastography," Biomed. Opt. Express **12**(3), 1725–1745 (2021).
56. J. Li, E. Pijewska, Q. Fang, M. Szkulmowski, and B. F. Kennedy, "Analysis of strain estimation methods in phase-sensitive compression optical coherence elastography," Biomed. Opt. Express **13**(4), 2224–2246 (2022).
57. J. Lu, A. J. Deegan, Y. Cheng, T. Liu, Y. Zheng, S. P. Mandell, and R. K. Wang, "Application of OCT-derived attenuation coefficient in acute burn-damaged skin," Lasers Surg. Med. **53**(9), 1192–1200 (2021).
58. P. Tang, M. A. Kirby, N. Le, Y. Li, N. Zeinstra, G. N. Lu, C. E. Murry, Y. Zheng, and R. K. Wang, "Polarization sensitive optical coherence tomography with single input for imaging depth-resolved collagen organizations," Light: Sci. Appl. **10**(1), 237 (2021).
59. P. Abraham, B. Fromy, S. Merzeau, A. Jardel, and J. L. Saumet, "Dynamics of local pressure-induced cutaneous vasodilation in the human hand," Microvasc. Res. **61**(1), 122–129 (2001).
60. B. Murphy-Chutorian, G. Han, and S. R. Cohen, "Dermatologic manifestations of diabetes mellitus: a review," Endocrinol. Metab. Clin. North Am. **42**(4), 869–898 (2013).

61. S. Laurent, C. Agabiti-Rosei, R. M. Bruno, and D. Rizzoni, "Microcirculation and macrocirculation in hypertension: a dangerous cross-link?" Hypertension **79**(3), 479–490 (2022).
62. I. Bentov and M. J. Reed, "The effect of aging on the cutaneous microvasculature," Microvasc. Res. **100**, 25–31 (2015).
63. C. H. Chen and P. D. Henry, "Atherosclerosis as a microvascular disease: impaired angiogenesis mediated by suppressed basic fibroblast growth factor expression," Proc Assoc Am Physicians **109**(4), 351–361 (1997).
64. R. Rosenberry and M. D. Nelson, "Reactive hyperemia: a review of methods, mechanisms, and considerations," Am. J. Physiol. Regul. Integr. Comp. Physiol. **318**(3), R605–R618 (2020).
65. Z. Xie, G. Wang, Y. Cheng, Q. Zhang, M. N. Le, and R. K. Wang, "Optical coherence tomography angiography measures blood pulsatile waveforms at variable tissue depths," Quant. Imaging Med. Surg. **11**(3), 907–917 (2020).
66. G. Stano, A. Di Nisio, A. Lanzolla, and G. Percoco, "Additive manufacturing and characterization of a load cell with embedded strain gauges," Precis. Eng. **62**, 113–120 (2020).